Int. J. Heat Mass Transfer. Vol. 31, No. 4, pp. 695–707, 1988
Printed in Great Britain

0017–9310/88 $3.00 + 0.00

A numerical study of three-dimensional natural convection in a horizontal porous annulus with Galerkin method

Y. F. RAO
Department of Energy Conversion Engineering, Interdisciplinary School of Engineering Science, Kyushu University, Fukuoka 816, Japan

and

K. FUKUDA and S. HASEGAWA
Department of Nuclear Engineering, Faculty of Engineering, Kyushu University, Fukuoka 812, Japan

(*Received* 17 *April* 1987)

Abstract—A Galerkin scheme is developed to study the three-dimensional natural convection in a fluid-saturated porous annulus heated from the inner surface. In addition to the two-dimensional multiple solutions reported in the authors' previous paper, three-dimensional solutions are obtained; the secondary cells, with streaklines of the three-dimensionally closed co-axial double helices, are found extending along the axial direction in the top region of the annulus. This brings about an increased maximum local heat transfer coefficient, which consequently enhances overall heat transfer compared with that for the two-dimensional unicellular flow.

1. INTRODUCTION

IN A PREVIOUS paper [1] the authors developed a two-dimensional (2-D) Galerkin scheme and investigated natural convection in a horizontal porous annulus and its related bifurcation phenomena. It was pointed out that besides solutions of the simple unicellular flows there exists more than one branching solution at higher Ra which yields overall heat transfer rates coincident better with experimental data. However, experimental measurements by Caltagirone [2] of the temperatures along a generatrix at the top of the annulus revealed a wave-like distribution, indicating the existence of a three-dimensional (3-D) cellular flow extending in the axial direction. He reported that the 2-D flow existed only at low Ra. Takata's measurement [3], though with a limited length in the axial direction, also confirmed the claim. Despite this three-dimensionality of the flow in the upper part of the annulus, however, numerical works in the literature [4–12] have all treated the problem with 2-D models, and no results have been presented to interpret the structure of this flow pattern. Caltagirone [2] described a program based on the finite-element method but could neither obtain convergent solutions nor carry out enough time steps to eliminate the influence of the possible strong initial perturbations; this was attributed to the capacity of computers at that time. In ref. [13] the authors developed a numerical scheme based on the finite-difference (SOR) method and obtained 3-D results in an inclined annulus with finite axial length. The formation of that flow pattern, however, is due to the presence of the component of the gravitational force in the axial direction, and it is therefore different from the flows in a horizontal annulus, where no such force exists and 3-D flow is thought to be induced by the instability due to a reverse temperature gradient at the top of the annulus as in the case of the Benard problem. Only 2-D results were obtained for the horizontal case [13]. As will be discussed later, this appears to be due to the fact that the use of the converged solutions obtained at lower Ra as initial conditions minimized an axial perturbation inherently produced by an SOR scheme, and thus prevented the flow from becoming 3-D.

In the present work, a 3-D Galerkin scheme is developed. The temperature as well as the components of the vector potential of velocity are expanded with a series of orthogonal eigenfunctions similar to those the authors developed in the 2-D scheme [1]. The scalar product is adopted to form residual equations in terms of the components of the vector potential, though the vector product has usually been adopted in 3-D Galerkin schemes dealing with the same problems of natural convection in enclosures [17, 18]. Discussions are made to show that the latter is just a special case of the former and the unconditional use of the vector product in Galerkin procedures may lead to significant errors.

In the same way as in the authors' previous work

NOMENCLATURE

a $\ln R/\pi$
A_{ijk} amplitude of the mode (i,j,k) of ψ_r
B_{ijk} amplitude of the mode (i,j,k) of ψ_ϕ
C_{ijk} amplitude of the mode (i,j,k) of ψ_z
C constants defined in Appendix B
D_x Dirichelet function
g gravitational acceleration
Ga $1/[\beta(\hat{T}_{in}-\hat{T}_o)]$
L dimensionless axial width of three-dimensional spiral flow, scaled by the inner radius
N_i, N_j, N_k cutoff numbers
Nu local Nusselt number
$\overline{Nu}$ average Nusselt number
P pressure
$\hat{r}$ radius distance
r coordinate in radius direction, scaled by $\hat{r}_{in}$
R ratio of the outer to the inner radius
Res residual in scalar form, equation (20)
Res residual in vector form, equation (22)
Ra Rayleigh number, $g\beta\kappa\hat{r}_{in}(\hat{T}_{in}-\hat{T}_o)/\alpha_{eq}\nu$
$\hat{T}$ temperature
T_{ijk} amplitude of the mode (i,j,k) of the dimensionless temperature θ
t time
$\mathbf{v}$ velocity vector
V_r, V_ϕ, V_z velocity components in the direction of the suffix
z coordinate along the axis of the annulus, scaled by $\hat{r}_{in}$.

Greek symbols
α_{eq} equivalent thermal diffusivity of the saturated porous medium
β thermal expansion coefficient of the fluid
δ Kronecker delta
Θ dimensionless temperature, $(\hat{T}-\hat{T}_o)/(\hat{T}_{in}-\hat{T}_o)$
θ dimensionless temperature defined by $\Theta-(1-\ln r/\ln R)$
κ permeability
λ direction vector $[-\cos\phi, \sin\phi, 0]$
ν kinematic viscosity of the fluid
ϕ angular coordinate measured from downward vertical axis
ψ vector potential of velocity
$\psi_r, \psi_\phi, \psi_z$ components of vector potential in the direction of the suffix.

Subscripts
in inner
o outer
(I,J,K); (i,j,k); (l,m,n) modes of dimensionless temperature, velocity or its vector potential
α mode $(I, |m-j|, |n-k|)$
β mode $(i, |j|, |k|)$.

Other symbols

$$\nabla \quad \left(\frac{\partial}{\partial r}, \frac{1}{r}\frac{\partial}{\partial \phi}, \frac{\partial}{\partial z}\right)$$

$$\nabla^2 \quad \frac{1}{r}\frac{\partial}{\partial r}r\frac{\partial}{\partial r}+\frac{1}{r^2}\frac{\partial^2}{\partial \phi^2}+\frac{\partial^2}{\partial z^2}$$

$$\sum_{\substack{l=1\\ i+l=\text{odd}}} \quad \sum_{i=1,3,\ldots} \text{ when } l \text{ is even}; \quad \sum_{i=2,4,\ldots} \text{ when } l \text{ is odd}$$

$$\sum_{\substack{j=1\\ j+m=\text{even}}} \quad \sum_{j=2,4,\ldots} \text{ when } m \text{ is even}; \quad \sum_{j=1,3,\ldots} \text{ when } m \text{ is odd}$$

$\langle\ \rangle$ volume integration over the annular space,

$$\int_1^R \int_0^\pi \int_0^L dr(r\,d\phi)\,dz.$$

[1], several initial conditions, including uniform temperature distributions or pure conduction solutions with and without perturbations, are adopted and their effects on determining final solutions are discussed. A randomly distributed perturbation is also introduced to obtain information about which of the branching solutions is preferred. The structure of the 3-D flow is clarified and its influence on the local and overall heat transfer examined, which is expected to cast a new light on the problem.

2. ANALYSES

2.1. *Formulation of the problem*

Consider a horizontal porous layer bounded by cylinders with its inner surface heated. The numerical model is shown in Fig. 1, where the gap between the cylinders is filled with a fluid-saturated porous medium. The inner and the outer surface, of dimensionless radii 1 and R, are maintained at different uniform dimensionless temperatures 1 and 0, respectively. The gravitational force on the system exerts vertically downward. Cylindrical coordinates are utilized, where ϕ is measured from the down vertical, r from the axis and z along the axis. Due to the symmetry of the boundary conditions and the gravitational force, the flow in the annulus is assumed to be symmetrical about the vertical symmetry plane. Since no external force exerts in the z-direction, the possible 3-D steady-state flows should take the cellular form with symmetry planes normal to the axis, planes I and II as shown in Fig. 1. It should be noted that in the Darcy problem, the boundary conditions at these planes are the same as the symmetry conditions.

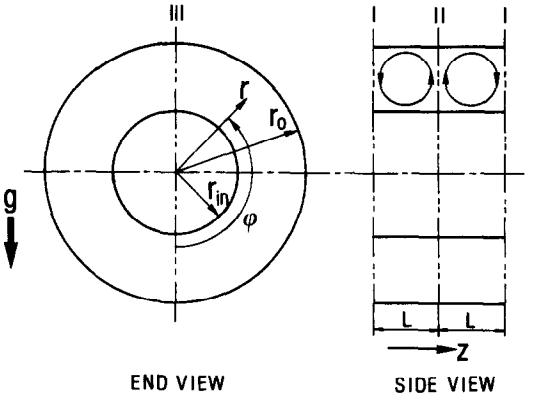

FIG. 1. Flow geometry and coordinate system.

The governing equations, the conservation of mass, Darcy's law and the conservation of energy, are given in equations (1)–(3), which are the same as we used in the previous paper [1]

$$\nabla \cdot \mathbf{v} = 0 \tag{1}$$

$$\nabla P - Ra\,\boldsymbol{\lambda}\Theta + Ra\,Ga\,\boldsymbol{\lambda} + \mathbf{v} = 0 \tag{2}$$

$$-(\mathbf{v}\cdot\nabla)\Theta + \nabla^2\Theta = \partial\Theta/\partial t \tag{3}$$

where, $\boldsymbol{\lambda} = [-\cos\phi, \sin\phi, 0]$ indicates the unit vector in the down vertical direction. For convenience, we replace Θ by $\theta = \Theta - (1 - \ln r/\ln R)$. Thus equations (2) and (3) are rewritten as

$$\nabla P^* + \begin{bmatrix} \cos\phi/\ln R \\ 0 \\ 0 \end{bmatrix} - \lambda\theta + \frac{1}{Ra}\mathbf{v} = 0 \tag{4}$$

$$-(\mathbf{v}\cdot\nabla)\theta + \frac{V_r}{r\ln R} + \nabla^2\theta = \partial\theta/\partial t \tag{5}$$

where $P^* = P/Ra - Ga\,r\cos\phi + r(1-\ln r/\ln R)\cos\phi$. The boundary conditions to be satisfied are

$$\begin{aligned} V_r &= \theta = 0, \quad \text{at } r = 1, R \\ V_\phi &= \partial\theta/\partial\phi = 0, \quad \text{at } \phi = 0, \pi \\ V_z &= \partial\theta/\partial z = 0, \quad \text{at } z = 0, L. \end{aligned} \tag{6}$$

The equation of continuity is satisfied identically by introducing the vector potential

$$\mathbf{v} = \nabla \times \boldsymbol{\psi}. \tag{7}$$

Taking the curl of the equation of Darcy's law, we eliminate the pressure term and obtain the following equations:

$$\nabla^2\psi_r - \left[\frac{\psi_r}{r^2} + \frac{2}{r^2}\frac{\partial\psi_\phi}{\partial\phi}\right] = Ra\sin\phi\frac{\partial\theta}{\partial z} \tag{8}$$

$$\nabla^2\psi_\phi - \left[\frac{\psi_\phi}{r^2} - \frac{2}{r^2}\frac{\partial\psi_r}{\partial\phi}\right] = Ra\cos\phi\frac{\partial\theta}{\partial z} \tag{9}$$

$$\nabla^2\psi_z = -Ra\left(\sin\phi\frac{\partial\theta}{\partial r} + \cos\phi\frac{1}{r}\frac{\partial\theta}{\partial\phi}\right). \tag{10}$$

The corresponding boundary conditions from Hirasaki and Hellums [14] are

$$\begin{aligned} &\frac{1}{r}\frac{\partial}{\partial r}(r\psi_r) = \psi_\phi = \psi_z = \theta = 0, \quad \text{at } r = 1, R \\ &\psi_r = \frac{\partial\psi_\phi}{\partial\phi} = \psi_z = \frac{\partial\theta}{\partial\phi} = 0, \quad \text{at } \phi = 0, \pi \\ &\psi_r = \psi_\phi = \frac{\partial\psi_z}{\partial z} = \frac{\partial\theta}{\partial z} = 0, \quad \text{at } z = 0, L. \end{aligned} \tag{11}$$

2.2. *Galerkin scheme*

The Galerkin method has been described in general cases in refs. [15, 16]. In the present study, the temperature and the three components of the vector potential are expanded as follows:

$$\tilde{\psi}_r = \Sigma_1 A_{ijk}\psi_{r_{ijk}} = \Sigma_1 A_{ijk}\frac{1}{r}\cos\left(\frac{i}{a}\ln r\right)\sin j\phi\sin\frac{k\pi}{L}z \tag{12}$$

$$\tilde{\psi}_\phi = \Sigma_2 B_{ijk}\psi_{\phi_{ijk}} = \Sigma_2 B_{ijk}\frac{1}{r}\sin\left(\frac{i}{a}\ln r\right)\cos j\phi\sin\frac{k\pi}{L}z \tag{13}$$

$$\tilde{\psi}_z = \Sigma_3 C_{ijk}\psi_{z_{ijk}} = \Sigma_3 C_{ijk}\sin\left(\frac{i}{a}\ln r\right)\sin j\phi\cos\frac{k\pi}{L}z \tag{14}$$

$$\tilde{\theta} = \Sigma_4 T_{ijk}\theta_{ijk} = \Sigma_4 T_{ijk}\frac{1}{r}\sin\left(\frac{i}{a}\ln r\right)\cos j\phi\cos\frac{k\pi}{L}z \tag{15}$$

where, '~' denotes a truncated series, and

$$\Sigma_1 = \sum_{011} = \sum_{i=0}^{N_i}\sum_{j=1}^{N_j}\sum_{k=1}^{N_k}; \quad \Sigma_2 = \sum_{101}; \quad \Sigma_3 = \sum_{110}; \quad \Sigma_4 = \sum_{100}. \tag{16}$$

These trial functions were formed from an extension of the 2-D ones developed in the previous work [1]; they are orthogonal in the annular space and satisfy the boundary conditions. Identically corresponding to equations (12)–(14) are the velocity expansions that satisfy the boundary conditions and the continuity equation:

$$\tilde{V}_r = \sum_{100}\left(jC_{ijk} - \frac{k\pi}{L}B_{ijk}\right) \times \frac{1}{r}\sin\left(\frac{i}{a}\ln r\right)\cos j\phi\cos\frac{k\pi}{L}z \tag{17}$$

$$\tilde{V}_\phi = \sum_{010}\left(\frac{k\pi}{L}A_{ijk} - \frac{i}{a}C_{ijk}\right) \times \frac{1}{r}\cos\left(\frac{i}{a}\ln r\right)\sin j\phi\cos\frac{k\pi}{L}z \tag{18}$$

$$\tilde{V}_z = \sum_{001}\left(\frac{i}{a}B_{ijk} - jA_{ijk}\right) \times \frac{1}{r^2}\cos\left(\frac{i}{a}\ln r\right)\cos j\phi \sin\frac{k\pi}{L}z. \quad (19)$$

The Galerkin method is based on the idea that a given function (here residual) must be zero everywhere in a given space if it is normal to every term of a complete series (here trial functions) in the space. The procedure is practically conducted by multiplying the residual with the trial functions and then integrating over the space. In the published works [17, 18] dealing with 3-D natural convection in horizontal or inclined porous boxes, the vector product using the velocity vector has been adopted to form the residual equation. In the present study, scalar products using components of vector potential are used. Discussions are made on differences and relations between the two procedures in the following and in the Appendices.

(a) Residual equations by scalar product (using ψ_r, ψ_ϕ, ψ_z and θ). Inserting the truncated series of equations (12)–(15) into equation (8), we obtain an expression for the scalar residual

$$\mathrm{Res}_r = \nabla^2\tilde{\psi}_r - \left[\frac{\tilde{\psi}_r}{r^2} + \frac{2}{r^2}\frac{\partial\tilde{\psi}_\phi}{\partial\phi}\right] - Ra\sin\phi\frac{\partial\tilde{\theta}}{\partial z}. \quad (20)$$

The Galerkin procedure gives a set of simultaneous equations

$$\langle \mathrm{Res}_r \cdot \psi_{r_{lmn}}\rangle = 0 \qquad l = 0, N_i; \quad m = 1, N_j; \quad n = 1, N_k \quad (21)$$

where the angular brackets mean integration over the annular space. The other two sets of equations for Res_ϕ and Res_z are obtained in the same way. Thus, we have three sets of equations for the unknowns A_{ijk}, B_{ijk}, and C_{ijk}.

(b) Residual equations by vector product (using $\mathbf{v}$–θ formulation). Inserting a truncated series $\tilde{\mathbf{v}}$ directly into the equation of Darcy's law, equation (4), we have a residual in vector form

$$\mathbf{Res} = \nabla P^* + \begin{bmatrix}\cos\phi/\ln R\\ 0\\ 0\end{bmatrix} - \lambda\tilde{\theta} + \frac{1}{Ra}\tilde{\mathbf{v}}. \quad (22)$$

The corresponding set of residual equations is

$$\langle \mathbf{Res}\cdot\mathbf{v}_{lmn}\rangle = 0 \qquad l = 1, N_i; \quad m = 0, N_j; \quad n = 0, N_k. \quad (23)$$

Since equation (23) produces only one set of residual equations, the vector trial function must have the following form:

$$\mathbf{v} = \sum E_{ijk}\mathbf{v}_{ijk} = \sum E_{ijk}\begin{bmatrix}V_{r_{ijk}}\\ V_{\phi_{ijk}}\\ V_{z_{ijk}}\end{bmatrix}. \quad (24)$$

One choice is to let $A_{ijk} = B_{ijk} = C_{ijk} = E_{ijk}$ in equations (17)–(19). However, we consider herein the following trial functions which are very close to those usually adopted in the literature [17, 18]:

$$\tilde{\mathbf{v}} = \sum E_{ijk} \times \begin{bmatrix} -\left(\frac{k^2\pi^2}{L^2} + j^2\right)\frac{1}{r}\sin\left(\frac{i}{a}\ln r\right)\cos j\phi\cos\frac{k\pi}{L}z\\ j\left(\frac{i}{a}\right)\frac{1}{r}\cos\left(\frac{i}{a}\ln r\right)\sin j\phi\cos\frac{k\pi}{L}z\\ \frac{k\pi}{L}\left(\frac{i}{a}\right)\frac{1}{r^2}\cos\left(\frac{i}{a}\ln r\right)\cos j\phi\sin\frac{k\pi}{L}z\end{bmatrix}. \quad (25)$$

It is a combination of two sets of trial functions, each involving a pair of velocity components and satisfying the boundary conditions and the continuity equation in corresponding 2-D (r–ϕ or r–z) planes.

We can easily find that equation (25) is a special case of equations (17)–(19) under the conditions

$$A_{ijk} = \frac{(i/a)}{(k\pi/L)^2 + j^2}\left[jB_{ijk} + \frac{k\pi}{L}C_{ijk}\right] \quad (26)$$

which yields E_{ijk} in equation (24) as

$$E_{ijk} = \frac{1}{(k\pi/L)^2 + j^2}\left[\frac{k\pi}{L}B_{ijk} - jC_{ijk}\right]. \quad (27)$$

Now, it is found that this condition has an equivalent

$$\frac{1}{r}\frac{\partial V_z}{\partial\phi} - \frac{1}{r^2}\frac{\partial V_\phi}{\partial z} = 0 \quad (28)$$

which is not the case in the present problem unless the flow pattern is two-dimensional. As will be shown later, trial functions (25) cannot produce correct solutions for 3-D flow. In Appendix A, a further discussion is also made for the case of an inclined box, which leads to the conclusion that this formulation is correct only in the horizontal case or in the case of 2-D flow.

2.3. *Solution procedure*

Evaluating every term of the inner products in the residual equation (21), which corresponds to equation (8), we obtain equations for the amplitudes of the modes, A_{lmn}, B_{lmn}, C_{lmn}. Those corresponding to equations (9) and (10) are also obtained in the same way. They are as follows:

$$\sum_{i=0}^{N_i} C_1 A_{imn} + \sum_{i=1}^{N_i} C_2 B_{imn} = \sum_{\substack{i=1\\ i+l=\text{odd}}}^{N_i} C_3[(1+\delta_{m1})T_{i,m-1,n} - T_{i,m+1,n}] \qquad l = 0, N_i; \quad m = 1, N_j; \quad n = 1, N_k \quad (29)$$

$$\sum_{i=1}^{N_i} C_4 B_{imn} + \sum_{i=0}^{N_i} C_5 A_{imn} = \sum_{\substack{j=1 \\ j+m=\text{even}}}^{N_i} C_6 T_{ljn}$$

$$l = 1, N_i; \quad m = 0, N_j; \quad n = 1, N_k \quad (30)$$

$$\sum_{i=1}^{N_i} C_7 C_{imn} = \sum_{\substack{i=1 \\ i+l=\text{odd}}}^{N_i} C_8[(1+\delta_{m1})T_{i,m-1,n} - T_{i,m+1,n}]$$

$$+ C_9[(m+\delta_{m1})T_{l,m-1,n} + mT_{l,m+1,n}] + C_{10}$$

$$l = 1, N_i; \quad m = 1, N_j; \quad n = 0, N_k. \quad (31)$$

Similarly, from the energy equation we have

$$C_{11}\frac{\mathrm{d}}{\mathrm{d}t}T_{lmn} = \sum_{i=1}^{N_i}\left[C_{12}\left(mC_{imn} - \frac{n\pi}{L}B_{imn}\right) + C_{13}T_{imn}\right]$$

$$+ \sum_{\substack{i=0 \\ l=0}}^{N_i} \sum_{\substack{j= \\ m-N_j}}^{N_j} \sum_{\substack{k= \\ n-N_k}}^{N_k} [C_{14}C_\alpha + C_{15}B_\alpha + C_{16}A_\alpha]T_\beta$$

$$l = 1, N_i; \quad m = 0, N_j; \quad n = 0, N_k \quad (32)$$

where $\alpha = (I, |m-j|, |n-k|)$ and $\beta = (i, |j|, |k|)$, and the coefficient functions appearing in these equations, i.e. C_1–C_{16}, are given in Appendix B. Equations (29)–(32), derived from the initial value problem (8)–(10) and (5), constitute a first-order non-linear ordinary differential system and are solved as follows. First, for a set of initial values of T_{lmn}, equations (29)–(31) are iteratively solved to determine the values of A_{lmn}, B_{lmn} and C_{lmn}; they are then used in integrating equation (32) to obtain T_{lmn}'s for the new time step. As can be found in Appendix B, the coefficient for A_{lmn}, i.e. $C_1(i = l)$, is much larger than the others on the left-hand side of equation (29), and the similar feature is also found in equations (30) and (31). As this makes the solutions converge very fast, two or three iterations are actually enough to obtain converged solutions with a maximum error of 0.001.

The time-marching integration is carried out with the rational Runge–Kutta method developed by Wambecq [19] as an explicit method for solving stiff ordinary differential equations, which is stable at much larger time intervals than the conventional Runge–Kutta method. The effectiveness of this method in integrating equations for natural convection problems was also confirmed in our previous work [1]. The radius ratio R is set to 2.0. The value of 0.94 is chosen as the cell width L for convenience of comparing with the experimental data available [2]. The time intervals used are between 0.003 and 0.01. Time-marching is continued until the relative change in the average Nusselt number becomes less than 0.0001. The CPU time for an average run with $N_i \times N_j \times N_k = 10 \times 13 \times 5$ is about 20 min with an FACOM-VP100 computer.

3. RESULTS AND DISCUSSION

3.1. *Comparison between the two Galerkin procedures*

To form the residual equations of Darcy's law, the above-mentioned two Galerkin procedures using either the scalar or the vector product are formulated and coded. The procedure using the scalar product, as given in equation (21), is proved to be computationally effective and to produce 3-D results which coincide with those obtained by a finite-difference method [13]. However, the procedure using the vector product, equation (23), fails to produce convergent 3-D results. When perturbations or converged solutions obtained from other methods are taken as initial values, the resulting solutions by the procedure either become two-dimensional or diverge fast. The validities of the two sets of trial functions, equations (12)–(14) (or identically equations (17)–(19)), and (25), are therefore examined by expanding a converged solution for a single cell of 3-D spiral flow which is obtained by a finite-difference method with a mesh grid of $21 \times 51 \times 21$ ($r \times \phi \times z$). If a series of trial functions is a complete set, the solution expanded with it approaches a real solution with increasing truncating number of the expansion. Thus the following average residual should approach zero

$$\mathrm{Res}_\phi = \left\langle (\nabla \times \tilde{\mathbf{v}})_\phi - Ra\cos\phi\frac{\partial\tilde{\theta}}{\partial z}\right\rangle \quad (33)$$

where $\tilde{\mathbf{v}}$ and $\tilde{\theta}$ are truncated series for either of the two expansions, and equation (33) is identically the same as the averaged residual of equation (9). Here Res_ϕ is chosen because ψ_ϕ gives the cellular convection in the r–z plane at the top of the annulus and is most sensitive to trial functions, and also because both $\cos\phi$ and $\partial\theta/\partial z$ have large values at the top, where 3-D flow occurs, so that $\langle Ra\cos\phi\,\partial\theta/\partial z\rangle$, which takes the same value for the two procedures, can be used as the scale factor for the residual. This avoided numerical integrating of the absolute value of the term in angular brackets, which would take much computer time for large cutoff numbers. In Fig. 2, the results are compared where N is set equal to $N_i = N_j = N_k$ for convenience. It is found that the series using trial functions for the scalar product, equations (12)–(14) or identically equations (17)–(19), gives a converged solution, whereas the series using trial functions for vector product (25) gives a diverged solution with increasing N. This indicates that the use of an incomplete series of trial functions may yield solutions that do not converge to the differential equation we attempt to solve.

3.2. *Multiple solutions corresponding to different initial conditions*

As described and discussed in our previous work dealing with a 2-D problem, the initial condition sometimes plays a determining role in the problem involving instability. It should be noted, however, that there is no general way for choosing initial conditions, particularly when stability is involved. Instability expected to occur in the present problem is mainly due to a reverse temperature gradient at the top of the annulus, as is similar to the case of the well-known

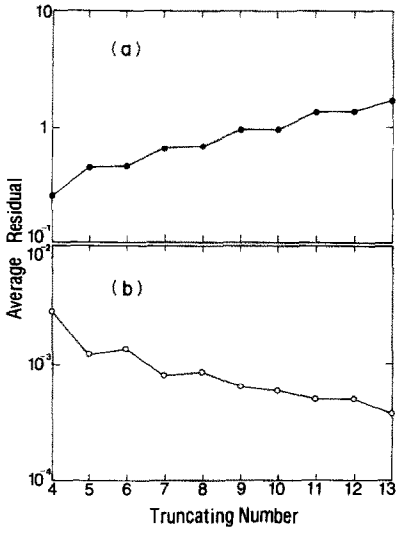

FIG. 2. Residuals for two Galerkin procedures: (a) by incomplete series equation (25); (b) by complete series equations (17)–(19).

Benard problem. In such a problem, an initial perturbation is necessary since the unstable change of flow patterns as well as the onset of convection are usually caused by small perturbations in nature; the use of the conduction state or a uniform temperature distribution as initial conditions may prevent these solutions from being obtained. The number of steady-state multiple solutions at a given *Ra* is an intrinsic feature of the problem and should be independent of initial conditions. However, there is no general method at present to determine the number in such a complicated non-linear problem; it should be analyzed case by case, and empirically in most cases. The simplicity of the geometric and boundary conditions in the present problem allow us to assume that the possible branching solutions take the form of secondary (multiple) cell patterns extending at the top region of the annulus in either circumferential or axial directions. The former involves reported 2-D branching solutions of multicellular flow [1]; and the latter involves a 3-D branching solution of a spiral flow which is treated in the present work.

Table 1 lists the initial conditions adopted. Since the velocity is set to zero, these conditions do not conflict with any of the governing equations. Types 1, 2 and 3 are 2-D ones corresponding to the conduction state or the uniform temperature distribution with and without 2-D oriented perturbations; they produce 2-D uni-, bi-, and tricellular flows as shown in Fig. 3. Type 4 corresponds to oriented 3-D perturbations, where $(-1)^j T_{1j1}$ are given values with the same sign so that a wavy distribution along the axial direction is formed at the top of the annulus ($\phi = \pi$). It generates 3-D flows the structures of which will be discussed later. In Table 2, dominant modes for 2- and 3-D branching solutions are listed in the order of their absolute values. Here, by 'mode (i, j, k)' we mean a harmonic component corresponding to one term in the Galerkin expansion; it specifies a flow pattern satisfying boundary conditions with wave numbers i, j, k in the r-, ϕ- and z-direction, respectively. We can find that among the branching solutions, common modes exist describing the main flow circulation which is nearly two-dimensional even for 3-D spiral flow; they are (1, 1, 0), (2, 0, 0), (2, 1, 0), (1, 2, 0), etc. Special modes, underlined in the table, also appear corresponding to different secondary flows occurring at the top region of the annulus. In the case of 3-D flow, modes $(1, j, 1)$ become dominant. It is found that the value of $(-1)^j T_{1j1}$ varies very regularly and has the same sign as shown in Fig. 4. This contributes to form a temperature distribution corresponding to a 3-D spiral flow.

3.3. *Stability of the multiple solutions*

Initial condition Type 5 was also introduced to find which of the branching solutions would be preferred under random initial conditions. When the amplitude of the random perturbation was small, the 2-D unicellular flow became dominant; while when the amplitude was large enough, above 0.001–0.02 varying with *Ra*, the 3-D flow appeared. Thus, the 2-D unicellular and the 3-D spiral flows seem to be more apt to become dominant than the other 2-D multicellular flows.

Table 1. Various initial conditions

Type 1 for 2-D unicellular	Type 2 for 2-D bicellular	Type 3 for 2-D tricellular	Type 4 for 3-D spiral flow	Type 5
(a) all $T_{ijk} = 0$	all $T_{ijk} = 0$ except $T_{130} = \varepsilon$, $T_{140} = -\varepsilon$, $T_{150} = \varepsilon$	all $T_{ijk} = 0$ except $T_{160} = \varepsilon$, $T_{170} = -\varepsilon$, $T_{180} = \varepsilon$, $T_{190} = -\varepsilon$	all $T_{ijk} = 0$ except $T_{101} = -\varepsilon$, $T_{111} = \varepsilon$, $T_{121} = -\varepsilon$, $T_{131} = \varepsilon$	Random distributions of perturbations adding to $\theta = 0$
(b) adding $T_{i00} = -\dfrac{2i}{\pi(a^2+i^2)}\left\{1 + \dfrac{2a[(-1)^i R - 1]}{\pi(a^2+i^2)}\right\}$ to the above initial conditions				

$\varepsilon(>0) = 0.001$–0.1: (a) conditions corresponding to pure or perturbed conduction state; (b) conditions corresponding to pure or perturbed uniform temperature distribution.

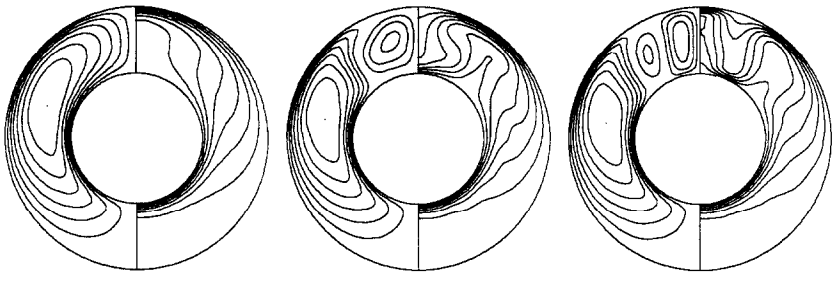

FIG. 3. Two-dimensional branching solutions which are the same as those obtained in the previous work [1].

Table 2. Dominant modes of multiple solutions for $Ra = 120$

2-D unicellular		2-D bicellular		2-D tricellular		3-D spiral flow	
Mode	T_{ijk}	Mode	T_{ijk}	Mode	T_{ijk}	Mode	T_{ijk}
1,1,0	−0.659	1,1,0	−0.508	1,1,0	−0.487	1,1,0	−0.561
2,0,0	−0.165	1,3,0	0.191	1,3,0	0.170	1,1,1	0.173
2,1,0	0.141	2,0,0	−0.185	2,0,0	−0.166	2,0,0	−0.161
1,2,0	0.134	1,4,0	−0.173	2,1,0	0.118	2,1,0	0.133
3,1,0	−0.103	2,1,0	0.161	1,7,0	−0.115	1,2,1	−0.128
2,2,0	−0.081	1,5,0	0.128	1,8,0	0.113	3,1,0	−0.107
1,0,0	−0.061	3,1,0	−0.110	1,2,0	−0.112	1,0,0	−0.104
		1,0,0	−0.109	1,0,0	−0.108	1,0,1	−0.096
		1,2,0	−0.085	3,1,0	−0.092	1,3,1	0.076
		1,6,0	−0.081	1,9,0	−0.090	2,2,0	−0.070

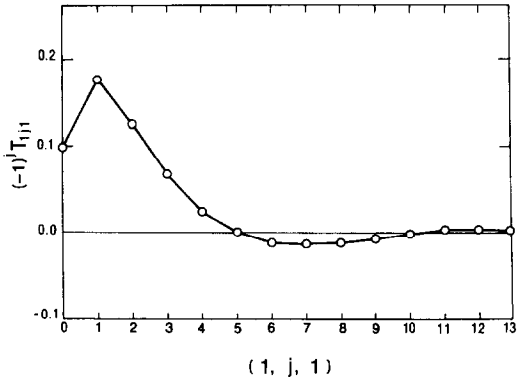

FIG. 4. Dominant modes of temperature $(1, j, 1)$ for $Ra = 150$, $L = 0.94$.

In previous work using the finite-difference method [13], 3-D results could not be obtained. This seems to be due to the fact that the use of converged solutions at a slightly lower *Ra* as initial conditions reduces the numerical perturbation of an artificial, axial temperature gradient, which is inherently introduced from the Gauss–Seidel iteration in the SOR method (see Appendix C). It is proved that unless their amplitudes are large enough, perturbations, either oriented or random, cannot result in branching solutions other than the unicellular one. This indicates that the transition of flow patterns from the basic 2-D unicellular to other branching solutions seems to be nonlinear and cannot be treated with the linear theory.

The bifurcation phenomenon discussed herein does not result from the use of the Galerkin scheme; the same multiple solutions can be obtained when similar initial perturbations are introduced to the scheme (described in ref. [13]) based on the finite-difference method. In previous experiments [2, 3], the flow was reported to be 2-D at lower *Ra* and 3-D at higher *Ra*. Nothing was reported related to the fact that more than one flow pattern exists at a given *Ra*. However, these experiments were mainly aimed at finding overall heat transfer rates and no attention was paid to the possibility of bifurcation. The authors therefore believe that further experimental work is needed to find whether the same bifurcation can be observed in the laboratory.

3.4. *Structure of the* 3-D *spiral flow*

Figure 5 shows the temperature variation along a generatrix at the top of the annulus. In this figure, the numerical result obtained with the Galerkin method is extended by symmetry and periodicity to involve more than one cell and compared with the measurement by Caltagirone [2]; agreement is qualitatively satisfactory. To confirm the validity of the numerical result further, it is also compared with that obtained by the finite-difference method, and a very good agreement is obtained. The average Nusselt numbers at the inner and outer surfaces deviate from each other by less than 1%.

The flow field and isothermal lines on several r–z

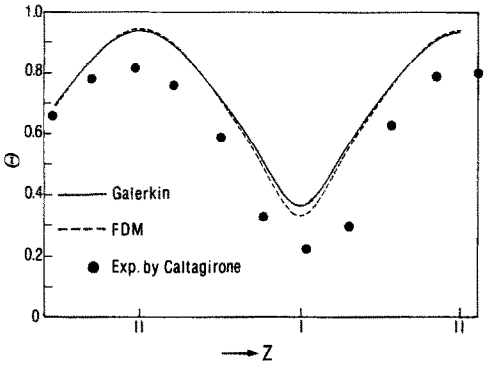

FIG. 5. Temperature distribution along a generatrix at the top with $r = 1.5$, $Ra = 150$, $L = 0.94$.

planes are shown in Fig. 6, where it is shown that the flow at the top region is very similar to a couple of Benard cells in a horizontal rectangular channel heated from below. This is due to the strong inverse temperature gradient there. These axially extending cellular flows become weaker at lower r–z planes, and at $\phi = 90°$ they tend to be difficult to identify. In Fig. 7, isotherms, flow fields and streaklines are plotted for two special symmetry planes, planes I and II, where the streaklines are planar. In plane I, the secondary cell adds a down-forward flow to the main circulation at the top of the annulus, and the temperature distribution is very like that for 2-D bicellular flow. It is found that velocities are nearly zero at two places, the top region near the inner cylinder and the center of the main circulation; and the streaklines show an interesting pattern: all of them end at the above two places. The center of the main circulation, located at (1.45, 106°), looks like a sink, but not a real one since the flow is three-dimensional. In plane II the isotherms and flow fields are very like those for the simple 2-D unicellular flow since the secondary flow is upforward at the top of the annulus, which is the same as the main circulation. The corresponding streaklines, however, show an interesting toroidal path starting at a point nearly the same as the 'sink' in plane I and spiraling towards the outer cylinder. It looks like a source. The streaklines in these symmetry planes will be helpful in our understanding of the 3-D spiral flow between them.

Figures 8(a)–(c) give streaklines of the 3-D spiral flow, which were obtained by three-dimensionally integrating the velocity field from a given starting point. As shown in Fig. 8(a), starting from a point at the top region, the streakline forms a co-axial double-helix which is similar to that observed in an inclined rectangular box [20]. While starting from near the 'sink' in plane I, the streakline spirals towards plane II along the axis linking the 'sink' and the 'source', which can also be considered as the axis of the main circulating flow. As it gets closer to plane II, it takes a toroidal path similar to that shown in Fig. 7 and will finally reach the outer layer directly affected by the double-helix cell at the top and then spirals back

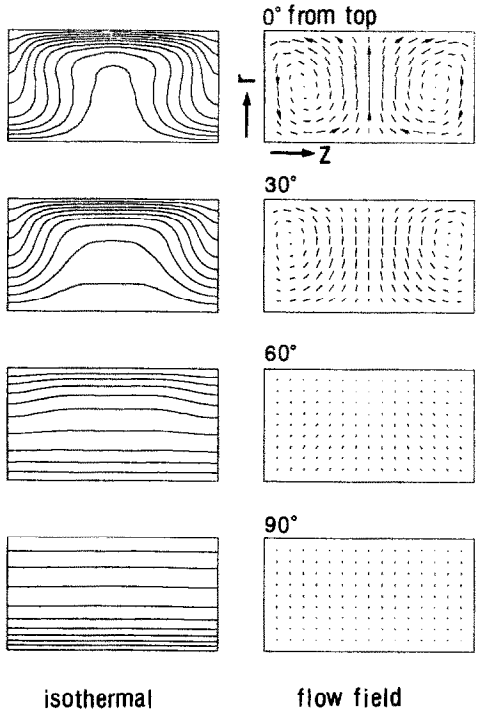

FIG. 6. Flow field and isotherms in the r–z planes for 3-D branching solution: $Ra = 100$, $L = 0.94$, $N_i \times N_j \times N_k = 10 \times 13 \times 5$.

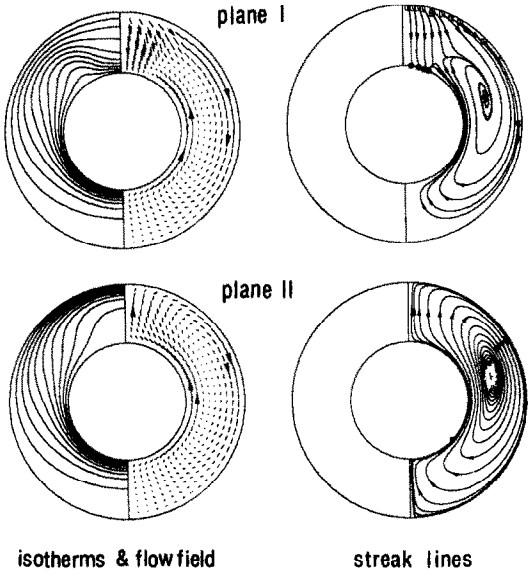

FIG. 7. Isotherms, flow fields and streaklines in symmetry planes I and II: $Ra = 100$, $L = 0.94$. Open squares and closed circles denote starting and end points, respectively.

towards plane I. This is shown in Fig. 8(b), where we can find that the streakline returns to within a very small distance from the starting point after spiraling several circuits of the toroidal path as numbered in order. The history of a toroidal circuit can also be found easily from the side view; the circuit generally becomes closer and closer to the bottom except the

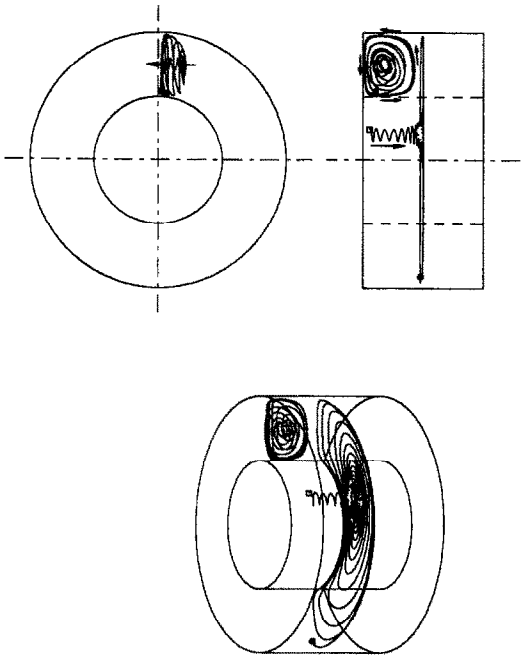

FIG. 8(a). Streaklines starting at points $(r, \phi, z) = (1.06, 174°, 0.20)$ and $(1.45, 110°, 0.10)$, $Ra = 100$, $L = 0.94$.

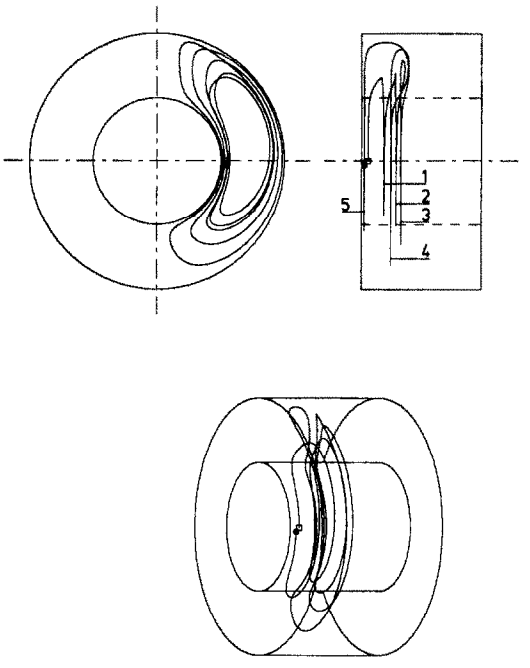

FIG. 8(c). Streakline starting at $(1.10, 90°, 0.10)$.

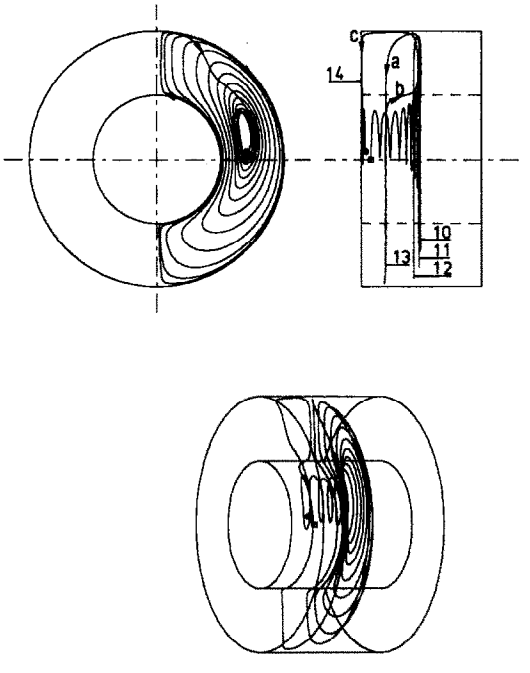

FIG. 8(b). Streakline starting at $(1.45, 90°, 0.15)$.

last one. Since the last toroidal circuit, No. 14, is in the very vicinity of plane I, it spirals towards the 'sink'–'source' axis along a path that can be found in Fig. 7. In Fig. 8(c), the starting point is chosen further from the axis; this results in a closed streakline with the same feature as that in Fig. 8(b), except that it does not get very close to plane II and is located in the remaining space of the streaklines in Figs. 8(a) and (b).

3.5. *Influence of the flow pattern on heat transfer*

In Fig. 9 local Nusselt numbers are plotted for 3-D spiral flows. It was found that the maximum Nusselt numbers in the upper part of the annulus are greatly increased owing to the 3-D cells extending along the axial direction. The average Nusselt numbers, however, are less affected since the 3-D flow occurs in a limited region at the top of the annulus. For the same reason, only a small difference can be found between transient results for 2- and 3-D flows, as shown in Fig. 10.

In Fig. 11, steady-state Nusselt numbers are plotted against *Ra* for 2- and 3-D branching solutions. Two-dimensional multicellular flows, the bi- and tricellular ones, agree better with experimental data, but they proved less preferred than the other branching solutions—the 3-D spiral and 2-D unicellular flows. Although the experimental data available are also insufficient, the deviation from experimental data at higher *Ra* is thought to be possibly caused by the physical model using Darcy's law and the assumption of the uniform medium. Kaviany [21] examined the effect of non-Darcy terms, such as inertia and diffusion, but showed that those terms could not increase overall heat transfer rates numerically calculated. Muralidhar and Kulaki [11] examined the effect of a non-uniform distribution of porosity, showing that the 'channeling effect' caused by a high porosity near the wall would greatly increase the heat transfer. Despite that these problems remain, however, we believe that the 3-D results obtained in the present work reveal essential features and they are thus applicable even when the model is modified.

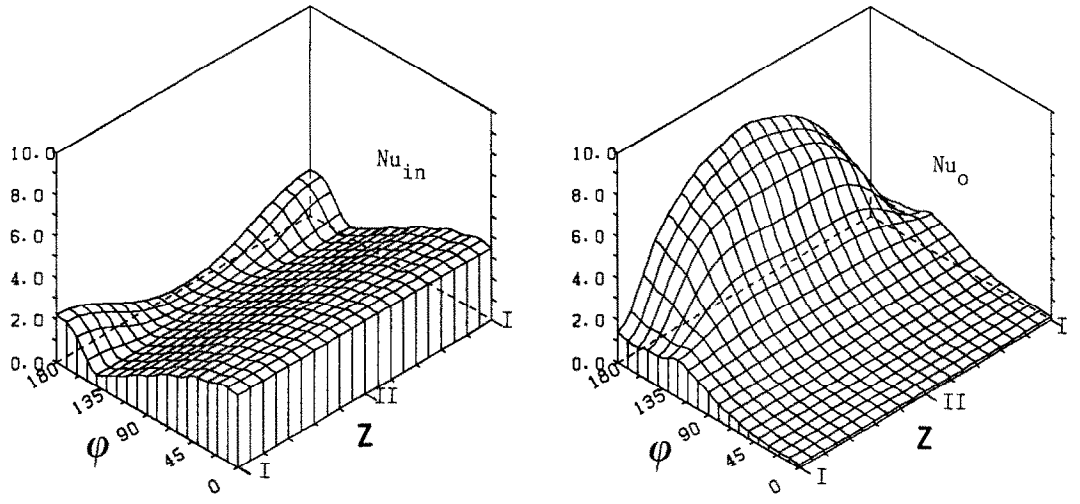

FIG. 9. Local Nusselt numbers at the inner and outer surfaces, $Ra = 100$, $L = 0.94$.

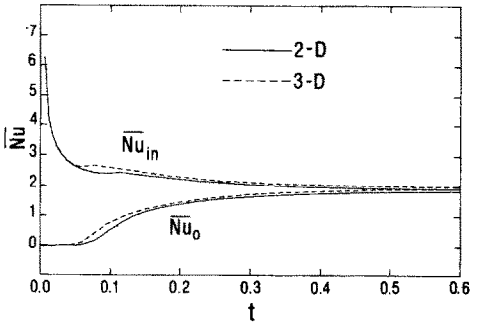

FIG. 10. Time variation of average Nusselt numbers for 2- and 3-D flows: $Ra = 100$.

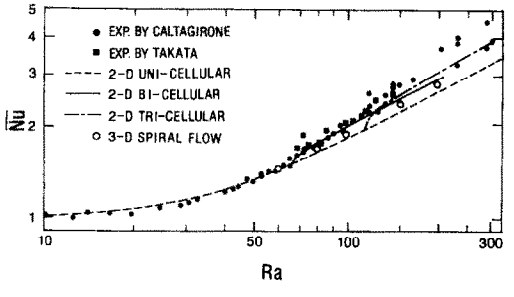

FIG. 11. Average Nusselt numbers for 2- and 3-D flows.

4. CONCLUDING REMARKS

Numerical results have been presented for the 3-D natural convection in a horizontal porous annulus heated from the inner surface. Conclusions drawn are summarized as follows.

(1) A Galerkin scheme using components of vector potential has been developed and compared with the Galerkin scheme using velocity vector; the latter was proved unsuitable.

(2) Multiple solutions have been obtained corresponding to initial perturbations. Results from random initial conditions indicate that the 2-D unicellular and the 3-D spiral flows seem more apt to become dominant than the other 2-D multicellular flows. It was found that 3-D flows cannot be obtained unless the initial perturbation is strong enough.

(3) The structure of a 3-D spiral flow has been clarified. At the upper part of the annulus, there exist secondary flows with closed streaklines of co-axial double helices as observed in inclined rectangular boxes.

(4) Compared with the 2-D unicellular flow, the 3-D spiral flow produces a higher maximum local heat transfer rate in the top region of the annulus, which enhances the overall heat transfer.

Acknowledgements—The authors would like to acknowledge the financial support from Japan Atomic Energy Research Institute (JARRI), under Grant No. 86139. Thanks are also due to Mr K. Kiku for his assistance in conducting some calculations.

REFERENCES

1. Y. F. Rao, K. Fukuda and S. Hasegawa, Steady and transient analyses of natural convection in a horizontal porous annulus with Galerkin method, 4th AIAA/ASME Thermophysics and Heat Transfer Conference, Boston, Vol. HTD-56, pp. 23–31 (1986). Also, *J. Heat Transfer* **109**, 919–927 (1987).
2. J. P. Caltagirone, Thermoconvective instabilities in a porous medium bounded by two concentric horizontal cylinders, *J. Fluid Mech.* **76**, 337–362 (1976).
3. Y. Takata, Three-dimensional natural convection in cylindric annuli, Doctor thesis (in Japanese), Kyushu University, Japan (1984).
4. R. Echigo, S. Hasegawa, S. Tottori, H. Shimomura and Y. Okamoto, An analysis on the radiative and free convective heat transfer in a horizontal annulus with permeable insulator, *Proc. 6th Int. Heat Transfer Conf.*, Vol. 3, pp. 385–390 (1978).
5. R. Echigo, S. Hasegawa, S. Tottori, H. Shimomura and Y. Okamoto, Studies on thermal insulation for a horizontal annulus at high temperature and high pressure (1st report, free convection in a horizontal annulus

with constant wall temperature), *Trans. J.S.M.E.* (in Japanese) **45**, 91–98 (1978).
6. P. J. Burns and C. L. Tien, Natural convection in porous media bounded by concentric spheres and horizontal cylinders, *Int. J. Heat Mass Transfer* **22**, 929–939 (1979).
7. T. Masuoka, N. Sakamoto and T. Katsuhara, Free convection heat transfer in a porous medium between horizontal concentric cylinders, *Trans. J.S.M.E.* (in Japanese) **46**, 919–926 (1980).
8. G. N. Facas and B. Farouk, Transient and steady-state natural convection in a porous medium between two concentric cylinders, *J. Heat Transfer* **105**, 660–663 (1983).
9. H. H. Bau, Low Rayleigh number thermal convection in a saturated porous medium bounded by two horizontal, eccentric cylinders, *J. Heat Transfer* **106**, 166–175 (1984).
10. H. H. Bau, Thermal convection in a horizontal, eccentric annulus containing a saturated porous medium—an extended perturbation expansion, *Int. J. Heat Mass Transfer* **27**, 2277–2287 (1984).
11. K. Muralidhar and F. A. Kulaki, Non-Darcy natural convection in a saturated horizontal porous annulus, 4th AIAA/ASME Thermophysics and Heat Transfer Conference, Boston, Vol. HTD-56, pp. 23–31 (1986).
12. K. Muralidhar, R. A. Baunchalk and F. A. Kulaki, Natural convection in a horizontal porous annulus with a step distribution in permeability, *J. Heat Transfer* **108**, 889–893 (1986).
13. K. Fukuda, Y. Takata, S. Hasegawa, S. Shimomura and K. Sanokawa, Three-dimensional natural convection in a porous medium between concentric inclined cylinders, 19th Natl Heat Transfer Conf., Vol. HTD-8, pp. 97–103 (1980).
14. G. J. Hirasaki and J. D. Hellums, A general formulation of the boundary conditions on the vector potential in three-dimensional hydrodynamic, *Q. Appl. Math.* **26**, 331–342 (1968).
15. B. A. Finlayson, *The Method of Weighted Residuals and Variational Principle*. Academic Press, New York (1972).
16. P. Gottieb and S. A. Orszag, *Numerical Analysis of Special Method: Theory and Applications*, Regional Conf. Series in Applied Maths, Vol. 26. Arrowsmith, Bristol (1977).
17. J. P. Caltagirone and S. Bories, Solutions and stability criteria of natural convection in an inclined porous layer, *J. Fluid Mech.* **155**, 267–287 (1985).
18. I. Altimir, Convection naturelle tridimensionnelle en milieu poreux sature par un fluide presentant un maximum de densite, *Int. J. Heat Mass Transfer* **27**, 1813–1824 (1984).
19. A. Wambecq, Rational Runge–Kutta methods for solving systems of ordinary differential equations, *Computing* **20**, 333–342 (1978).
20. H. Ozoe, N. Sato and S. W. Churchill, Experimental confirmation of the three-dimensional helical streak lines previously computed for natural convection in inclined rectangular enclosure, *Int. Chem. Engng* **19**, 454–462 (1979).
21. M. Kaviany, Non-Darcian effects on natural convection in porous media confined between horizontal cylinders, *Int. J. Heat Mass Transfer* **29**, 1513–1519 (1986).

APPENDIX A

Simply but now losing generality for comparing with refs. [17, 18], we consider natural convection in an inclined porous cubic box the heated surface of which is at an angle ϕ_0 to the horizontal plane. The equation of Darcy's law is written as

$$\nabla P + \mathbf{v} = Ra\,\Theta \begin{bmatrix} \sin\phi_0 \\ 0 \\ \cos\phi_0 \end{bmatrix}. \tag{A1}$$

The corresponding vector potentials are

$$\begin{aligned} \psi_x &= \sum b_{ijk} \cos i\pi x \sin j\pi y \sin k\pi z \\ \psi_y &= \sum c_{ijk} \sin i\pi x \cos j\pi y \sin k\pi z \\ \psi_z &= \sum a_{ijk} \sin i\pi x \sin j\pi y \cos k\pi z. \end{aligned} \tag{A2}$$

Since $\mathbf{v} = \nabla \times \boldsymbol{\psi}$ we have

$$\begin{aligned} V_x &= \sum \pi(ja_{ijk} - kc_{ijk}) \sin i\pi x \cos j\pi y \cos k\pi z \\ V_y &= \sum \pi(kb_{ijk} - ia_{ijk}) \cos i\pi x \sin j\pi y \cos k\pi z \\ V_z &= \sum \pi(ic_{ijk} - jb_{ijk}) \cos i\pi x \cos j\pi y \sin k\pi z. \end{aligned} \tag{A3}$$

In refs. [17, 18], expansions were adopted as follows:

$$\begin{aligned} \mathbf{v} &= \sum e_{ijk} \begin{bmatrix} V_{x_{ijk}} \\ V_{y_{ijk}} \\ V_{z_{ijk}} \end{bmatrix} \\ &= \sum e_{ijk} \begin{bmatrix} ik\pi^2 \sin i\pi x \cos j\pi y \cos k\pi z \\ jk\pi^2 \cos i\pi x \sin j\pi y \cos k\pi z \\ -(i^2+j^2)\pi^2 \cos i\pi x \cos j\pi y \sin k\pi z \end{bmatrix}. \end{aligned} \tag{A4}$$

We can easily find that equation (A4) is a special case of equation (A3) under the condition

$$a_{ijk} = \frac{k}{i^2+j^2}(ib_{ijk} + jc_{ijk}) \tag{A5}$$

which gives e_{ijk}'s in equation (A4) as

$$e_{ijk} = \frac{1}{i^2+j^2}(jb_{ijk} - ic_{ijk}). \tag{A6}$$

This condition has a physical meaning as

$$\Omega_z = (\nabla \times \mathbf{v})_z = 0. \tag{A7}$$

However, by taking the rotation of equation (A1), we have

$$(\nabla \times \mathbf{v})_z = \sin\phi_0\, Ra \frac{\partial \Theta}{\partial y} \tag{A8}$$

the right-hand side of which cannot be zero in the problem of 3-D convection in the inclined case, i.e. $\phi_0 \neq 0$ and $\partial\Theta/\partial y \neq 0$. From the results shown in Section 3, it is inferred that using this incomplete expansion series will prevent the results from converging with increasing truncating number.

APPENDIX B

Constants appearing in equations (29)–(32)

$$C_1 = \frac{\pi L}{2}[a^2m^2(4a^2+i^2+l^2)+2i^2l^2]X_3 + \delta_{il}\frac{an^2\pi^4}{8L}(1-\delta_{l0}) \tag{B1}$$

$$C_2 = -\frac{\pi m}{2} Lai(4a^2+i^2-l^2)X_3 \tag{B2}$$

$$C_3 = -Ra\frac{n\pi^2 ai}{4(i^2-l^2)} \tag{B3}$$

$$C_4 = \left\{\frac{\pi}{2} ilL\left[2\left(\frac{i^2}{a^2}+m^2\right)a^2 + 4a^2 + l^2 - i^2\right]X_3 + \frac{an^2\pi^4}{8L}\right\}(1+\delta_{m0}) \tag{B4}$$

$$C_5 = -\frac{\pi}{2} mLal(4a^2+l^2-i^2)X_3 \tag{B5}$$

$$C_6 = -Ra\frac{\pi^2}{4} na\left[\frac{m+1}{(m+1)^2+j^2} - \frac{m-1}{(m-1)^2-j^2}\right] \tag{B6}$$

$$C_7 = \left[-\frac{\pi^3}{L} n^2 a^2 il X_4 + \delta_{il} \frac{\pi^2}{8} La \left(\frac{l^2}{a^2} + m^2 \right) \right] (1+\delta_{n0}) \tag{B7}$$

$$C_8 = -Ra \frac{ilL\pi}{4(l^2-i^2)} (1+\delta_{n0}) \tag{B8}$$

$$C_9 = Ra \frac{\pi^2}{16} La (1+\delta_{n0}) \tag{B9}$$

$$C_{10} = Ra \frac{lL[1-R(-1)^l]}{2(a^2+l^2)} \delta_{m1} \delta_{n0} \tag{B10}$$

$$C_{11} = \frac{\pi^2}{8} La (1+\delta_{m0})(1+\delta_{n0}) \tag{B11}$$

$$C_{12} = \frac{L}{2} lai (1+\delta_{m0})(1+\delta_{n0}) X_5 \tag{B12}$$

$$C_{13} = \left[-\frac{\pi}{2} Lil(l^2+2a^2m^2+2a^2+i^2) X_3 - \delta_{il} \frac{an^2\pi^4}{8L} \right] (1+\delta_{m0})(1+\delta_{n0}) \tag{B13}$$

$$C_{14} = -\frac{\pi}{16} L \left[(m-j) X_6 + \frac{mI}{a} X_7 \right] \times (1+\delta_{0j})(1+\delta_{0k})(1+\delta_{nk}) D_{m-j} \tag{B14}$$

$$C_{15} = \frac{\pi^2}{16} \left[(n-k) X_6 + \frac{nI}{a} X_7 \right] \times (1+\delta_{0j})(1+\delta_{mj})(1+\delta_{0k}) D_{n-k} \tag{B15}$$

$$C_{16} = \frac{\pi^2}{16} X_7 (nj-mk)(1+\delta_{0j})(1+\delta_{0k}) D_{m-j} D_{n-k} \tag{B16}$$

where

$$D_x = \begin{cases} 1 & (x>0) \\ 0 & (x=0) \\ -1 & (x<0) \end{cases} \tag{B17}$$

stands for the Dirichelet function, and

$$X_0 = \left[1 - \frac{1}{R^2} (-1)^{I+i+l} \right] \tag{B18}$$

$$X_1 = \{[4a^2+(l+I+i)^2][4a^2+(l-I-i)^2]\}^{-1} \tag{B19}$$

$$X_2 = \{[4a^2+(l+I-i)^2][4a^2+(l-I+i)^2]\}^{-1} \tag{B20}$$

$$X_3 = \frac{\left[1 - \frac{1}{R^2} (-1)^{i+l} \right]}{[4a^2+(l+i)^2][4a^2+(l-i)^2]} \tag{B21}$$

$$X_4 = \frac{[1-R^2(-1)^{i+l}]}{[4a^2+(l+i)^2][4a^2+(l-i)^2]} \tag{B22}$$

$$X_5 = \frac{\left[1 - \frac{1}{R} (-1)^{i+l} \right]}{[a^2+(i+l)^2][a^2+(i-l)^2]} \tag{B23}$$

$$X_6 = \frac{al}{2} X_0 [(X_2-X_1)(4a^2+l^2+3I^2+3i^2) - 6Ii(X_2+X_1)] \tag{B24}$$

$$X_7 = -2a^2 l X_0 [I(X_2-X_1) - i(X_2+X_1)]. \tag{B25}$$

APPENDIX C

It is easy to see that, if the term $\partial\theta/\partial z$ on the right-hand side of equations (8) and (9) is initially set to zero as it should be under 2-D initial conditions, the results can only be two-dimensional. In the previous work [13], however, the axial perturbation was considered to exist due to the Gauss–Seidel iteration in the SOR method, in which discretization for the term was conducted as

$$\frac{\partial\theta}{\partial z} = \frac{\theta(r,\phi,z+\Delta z)^n - \theta(r,\phi,z-\Delta z)^{n+1}}{2\Delta z} \tag{C1}$$

where n stands for step number of iteration and Δz grid size in the axial direction. In equation (C1), we used values of temperatures at different iteration steps so that we introduced an artificial temperature gradient in the axial direction which would cause the onset of 3-D flow. However, the numerical gradient is small if the increase of Ra is small (although a change of the acceleration factor in the SOR method plays the same role). The reason that the 3-D results in the horizontal case could not be obtained in previous work [13] seem to be that the perturbation was suppressed since Ra was increased step by step as 0–25–50–100. Increasing Ra directly from 0 to 100 we obtained 3-D results. It is worth noting that simple iteration using

$$\frac{\partial\theta}{\partial z} = \frac{\theta(r,\phi,z+\Delta z)^n - \theta(r,\phi,z-\Delta z)^n}{2\Delta z} \tag{C2}$$

will prevent the artificial gradient from appearing, and moreover, the round-off error by a computer does not produce such perturbations since a computer truncates the calculation in every r–ϕ—here $z+\Delta z$ and $z-\Delta z$—planes exactly the same way. In this case, initial perturbations must be introduced to obtain branching solutions which are observed in the experiment. This was also confirmed in the case of rectangular geometry.

UNE ETUDE NUMERIQUE DE LA CONVECTION NATURELLE TRIDIMENSIONNELLE DANS UN ANNEAU POREUX HORIZONTAL PAR LA METHODE DE GALERKIN

Résumé—Un schéma de Galerkin est développé pour étudier la convection naturelle tridimensionnelle dans un espace annulaire saturé de fluide et chauffé par la surface interne. En supplément des solutions bidimensionnelles données par l'auteur dans un texte antérieur, on obtient des solutions tridimensionnelles; des cellules secondaires, avec des lignes proches des hélices doubles coaxiales, sont trouvées s'étendre le long de la direction axiale dans la région supérieure de l'espace annulaire. Ceci conduit à un accroissement du maximum du coefficient local de transfert de chaleur, ce qui améliore le transfert global par rapport à celui d'un écoulement bidimensionnel unicellulaire.

EINE NUMERISCHE UNTERSUCHUNG DER DREIDIMENSIONALEN NATÜRLICHEN KONVEKTION IN EINEM HORIZONTALEN PORÖSEN RING MIT DER GALERKIN-METHODE

Zusammenfassung—Eine Galerkin-Methode wird entwickelt, um die dreidimensionale natürliche Konvektion in einem fluidgesättigten porösen Ring, der an der inneren Fläche beheizt wird, zu untersuchen. Zusätzlich zu den zweidimensionalen Mehrfachlösungen, über die im vorhergehenden Artikel des Autors berichtet worden ist, erhält man dreidimensionale Lösungen. Es wurde herausgefunden, daß sich im oberen Teil des Rings in axialer Richtung Sekundärströmungszellen ausbilden. Die Streichlinien haben die Form einer dreidimensionalen geschlossenen koaxialen Doppel-Helix. Dies bewirkt einen erhöhten maximalen örtlichen Wärmeübergangskoeffizienten, der folglich den gesamten Wärmeübergangskoeffizienten gegenüber demjenigen für die zweidimensional einzellige Strömung verbessert.

ПРИМЕНЕНИЕ МЕТОДА ГАЛЕРКИНА ДЛЯ ЧИСЛЕННОГО ИССЛЕДОВАНИЯ ТРЕХМЕРНОЙ ЕСТЕСТВЕННОЙ КОНВЕКЦИИ В ГОРИЗОНТАЛЬНОМ ПОРИСТОМ КОЛЬЦЕВОМ КАНАЛЕ

Аннотация—Разработана схема для исследования методом Галеркина трехмерной естественной конвекции в насыщенном жидкостью пористом кольцевом канале с нагреваемой внутренней поверхностью. Помимо двумерных решений, которые были представлены аавторами в предыдущей работе, получены трехмерные решения. Найдено, что вторичные ячейки, которые имеют вид замкнутых коаксиальных сдвоенных спиралей, вытягиваются в осевом направлении в верхней части кольцевого канала. Это вызывает увеличение максимального значения локального коэффициента теплообмена, что, естественно, ведет к увеличению суммарного теплообмена по сравнению с тем, которое наблюдается при двумерном одноячеистом течении.